RSC Advances

PAPER

View Article Online
View Journal | View Issue

Cite this: *RSC Adv.*, 2025, **15**, 37597

In Situ kinetic analysis of perovskite halide exchange *via* laser trapping spectroscopy

Md. Jahidul Islam,* Saiful Islam and Md. Hafizul Islam

This study investigates the use of optical tweezers as a precise and non-invasive tool for probing chemical reaction kinetics, focusing specifically on halide exchange reactions in hybrid perovskite systems. A continuous-wave, tightly focused 1064 nm near-infrared laser beam was utilized to establish optical trapping conditions that precisely confine and manipulate the reaction interface between a methylammonium lead bromide ($MAPbBr_3$) microcrystal and a methylammonium iodide (MAI) solution. Upon laser irradiation, bromide ions within the perovskite lattice were progressively substituted by iodide ions, enabling controlled Br-to-I halide exchange. This compositional evolution was monitored in real time *via* optical spectroscopy by tracking the bandgap shift of the perovskite, which decreased from 2.29 eV (characteristic of pure $MAPbBr_3$) to 2.02 eV, confirming the formation of a mixed-halide phase, $MAPb(Br_{1-x}I_x)_3$ ($0 \leq x \leq 1$). Kinetic analysis of the bandgap evolution reveals a zero-order reaction behavior with a rate constant of 1.0×10^{-6} M min^{-1} and a calculated half-life of approximately 55 minutes. These findings demonstrate that optical tweezers can serve not only as a micromanipulation tool but also as an effective platform for *in situ* kinetic studies in solution-phase reactions. The approach enables detailed investigation of microscale reaction dynamics, delivering high spatial accuracy and second-scale temporal resolution for continuous monitoring of slow-evolving processes.

Received 25th August 2025
Accepted 30th September 2025

DOI: 10.1039/d5ra06340j

rsc.li/rsc-advances

1. Introduction

To achieve precise, non-invasive monitoring of chemical reactions, optical tweezers have emerged as a transformative tool.[1] Traditional techniques often disrupt the reaction environment, limiting the accuracy of kinetic studies.[2,3] In contrast, optical tweezers employ highly focused laser beams to confine and manipulate microscopic particles in a non-contact manner, enabling real-time observation of chemical transformations.[4,5] This study leverages a 1064 nm near-infrared laser to induce halide exchange in $MAPbBr_3$ hybrid perovskite microcrystals, specifically monitoring the Br-to-I substitution through bandgap modulation.[6] As the halide composition shifts, measurable changes in optical properties—captured *via* UV-vis absorption and photoluminescence spectroscopy—offer direct insight into reaction rates, mechanisms, and intermediate species.[7,8] The non-invasive nature of laser trapping provides high spatial resolution and precise environmental control, enabling unprecedented analysis of microscale chemical dynamics.[9] By detecting bandgap shifts, key kinetic parameters such as activation energy and reaction order can be extracted. Building on the foundational work of Arthur Ashkin, laser trapping now represents a powerful approach for studying chemical kinetics in confined systems, bridging the gap between physical manipulation and spectroscopic observation for advanced material and reaction analysis.[10]

Haifeng Yuan *et al.* (RIES group) have imaged heterogeneously distributed photo-active traps in perovskite single crystals, demonstrating how trap distributions affect local photophysics but without resolving the kinetics of halide exchange under optical perturbation.[11] Similarly, previous work has employed optical trapping to induce nucleation and growth of $MAPbX_3$ crystals in precursor solutions, showing that local concentration effects *via* optical forces are operative in perovskite systems.[12] Also, detailed quantitative imaging of anion exchange kinetics in single crystalline nanoplates (by confocal PL) has been reported, which provides useful benchmarks for rate constants and diffusion coefficients.[13] However, none of these studies have combined optical trapping with explicit determination of reaction order under continuous monitoring.

Our application of optical tweezers for real-time kinetic monitoring and localized bandgap engineering represents a significant advancement over conventional techniques. Most prior works in this field rely on bulk solution-phase reactions, thermal activation, or ensemble-averaged spectroscopic measurements.[12] In contrast, employing a tightly focused 1064 nm laser enables precise microscale manipulation and real-time monitoring of the halide exchange reaction. This enables localized reaction initiation and selective modification

Department of Chemistry, International University of Business Agriculture and Technology (IUBAT), Dhaka, Bangladesh. E-mail: jahidul.che@iubat.edu; dislam.chem@iubat.edu; hafizul.chem@iubat.edu

of individual $MAPbBr_3$ crystals, offering a novel route toward programmable perovskite bandgap tuning.

This study explores the novel application of optical trapping to investigate chemical reaction kinetics, focusing on reaction rate and order determination. By using laser tweezers to manipulate and concentrate reactants at the focal point, we enhance molecular interactions and accelerate reaction processes. Perovskite materials, especially hybrid metal halide perovskites (ABX_3), are chosen as model systems owing to their highly tunable optoelectronic properties and straightforward synthesis. Monitoring the time-dependent changes in reactant and product concentrations allows us to gain precise insights into kinetic behavior, demonstrating the potential of optical trapping in advancing reaction analysis techniques.

Hybrid metal halide perovskites, represented by the formula ABX_3, offer a versatile platform for optoelectronic applications. Here, A-site +1 oxidation state ion, B-site +2 oxidation state ion, and X is univalent halide ion (X^-). Fig. 1 illustrates the crystal structure of the ABX_3 perovskite. In earlier studies, halide-based materials have shown tunable optical band structures and absorption edges that are critical for tailoring optoelectronic performance in photonic applications.[13] Among the various modulation techniques, halide exchange is particularly attractive due to its relative ease and the significant impact it has on the material's optoelectronic properties.[14,15] The low activation energy for halide exchange, ranging from 0.25 to 0.58 eV, compared to the higher activation energies (2.1 eV) for cation exchange, makes it a more feasible approach. A similar dependency of electronic and optical properties on material composition has been observed in magnetic and semiconducting systems,[16] further validating the importance of halide modulation in band structure engineering.

In this study, $MAPbBr_3$ crystals were synthesized and subjected to laser-induced halide exchange using MAI solution, forming $MAPb(Br_{1-x}I_x)_3$ with tunable iodine content ($0 \leq x \leq 1$). Laser trapping at the crystal–solution interface accelerated Br^- to I^- substitution, observed *via* red-shifted emission spectra. Kinetic analysis based on MAI concentration and iodine incorporation revealed the reaction mechanism and rate parameters.

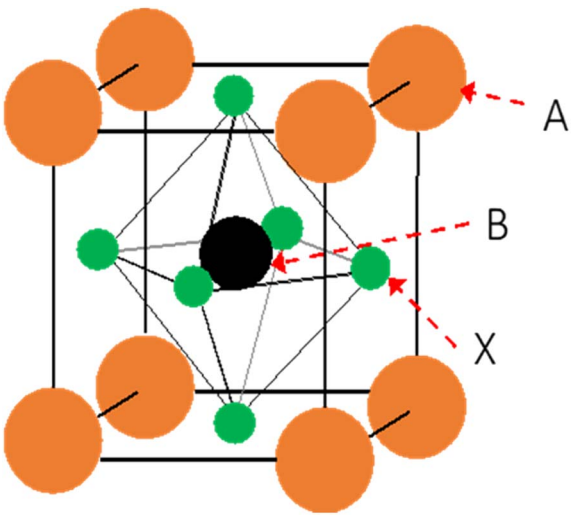

Fig. 1 Schematic diagram of molecular structure of ABX_3 hybrid lead halide perovskite. Where A = monovalent cation, B = divalent metal cation, X = monovalent halide ion.

Our main halide exchange chemical reaction is-

$$MAPBr_3 + MAI \rightarrow MAPb(Br_{1-x}I_x)_3 \quad (1)$$

Here $0 \leq x \leq 1$.

For determining the ratio of iodine in the inorganic metal halide perovskite $CsPb(Br_{1-x}I_x)_3$ composition utilizing the bandgap, there is well established equation developed by Y. Zhang *et al.*,[10]

$$E_g\{CsPb(Br_{1-x}I_x)_3\} = 2.34 - 0.27x - 0.29x^2 \quad (2)$$

Here, E_g – Bandgap of Br/I mixed halide perovskites, $E_g(CsPbBr_3) = 2.34$ eV, $E_g(MAPbI_3) = 1.76$ eV.

This equation was originally developed for the hybrid perovskite $MAPb(Br_{1-x}I_x)_3$ by K. Chen *et al.*[14]

$$E_g\{MAPb(Br_{1-x}I_x)_3\} = (1-x) \times E_g(MAPbBr_3) + x \times E_g(MAPbI_3) - b \times x \times (1-x) \quad (3)$$

Here, E_g – Bandgap of Br/I mixed halide perovskites, $E_g(MAPbBr_3) = 2.29$ eV, $E_g(MAPbI_3) = 1.6$ eV. b is bowing constant whose value is 0.57 eV.

Due to the large concentration difference between solid $MAPbBr_3$ and micromolar MAI solution, the reaction can be approximated as a unimolecular process, focusing on the consumption of MAI. The excess $MAPbBr_3$ maintains a constant concentration, while MAI undergoes significant changes. The reaction rate is thus expressed as

$$\text{Rate} = -(d[A])/dt = k[A_t]^n \quad (4)$$

where A_t is the MAI concentration at time t, and n is the reaction order. The change in $MAPb(Br_{1-x}I_x)_3$ bandgap serves as an indirect measure of MAI consumption, linking optical properties to reaction kinetics.

Previous reports have convincingly demonstrated that laser trapping can facilitate halide migration and induce Br-to-I exchange in hybrid perovskites by locally enhancing ionic mobility and filling lattice vacancies.[10,17,18] However, while the phenomenological aspects of laser–driven exchange are well documented, the kinetic framework underlying such processes has not been quantitatively established. In particular, the reaction order, which provides mechanistic insight into whether the exchange is governed by diffusion-limited, vacancy-mediated, or concentration–driven pathways, has not been addressed.

In this work, we explicitly determine that the Br-to-I halide exchange under laser trapping conditions follows a zero-order kinetic process, with a well-defined rate constant and half-life. This novel contribution provides the first quantitative mechanistic description of laser-induced halide exchange and distinguishes our study from prior observations that primarily reported the occurrence of exchange without kinetic evaluation.

However, unlike conventional diffusion-limited or thermal activation methods, our laser trapping approach allows non-invasive, spatially selective control of iodide incorporation in $MAPbBr_3$, thereby achieving localized and controllable bandgap narrowing.

2. Experimental

2.1. Experimental procedures: reagents and sample preparation

The reagents were used as received, without additional purification, for the halide exchange reaction. MABr (>97.0%) and MAI (>99.0%) were obtained from TCI, $PbBr_2$ (≥99.0%) from Sigma-Aldrich, and *N*,*N*-dimethylformamide (DMF, ≥98.50%), isopropanol (98.9%), and hexadecene (96.0%) from Wako. Micrometer-sized $MAPbBr_3$ perovskite crystals (~5 × 5 μm^2) were synthesized *via* a solvent evaporation method. For crystal growth, a 1.3 M $MAPbBr_3$ precursor solution was prepared by dissolving MABr and $PbBr_2$ in DMF under stirring at room temperature. The crystal size was controlled through drop-casting the precursor solution onto glass substrates. Within very short time (~1 minute), crystallization appears, and many small crystals formed in very close distance. When the size of the grown thin film crystal reached the 5 μm scale, we remove the excess solvent using tissue paper. For conducting trapping experiment, the 110 μM MAI solution prepared in mixed solvent of isopropanol/hexadecane, 1/100, v/v is poured to the reaction chamber which contain $MAPbBr_3$ crystal.

2.2. Experimental: optical arrangement for laser-induced halide exchange

For laser trapping and optical measurements, we followed standard protocols. Fig. 2 illustrates the optical system employed in this study. Experiments were carried out using a near-IR CW irradiation (wavelength λ = 1064 nm) as the irradiation root, coupled with a bottom-illumination microscope, a CCD imaging device, and a spectrometer. To regulate the NIR laser power, a half-wave plate in combination with a polarizing beam splitter was employed. The half-wave plate rotates the polarization of the linearly polarized laser beam, while the beam splitter selectively transmits horizontally polarized light and reflects vertically polarized light. Together, this arrangement enables fine control over the NIR laser power.

An inverted microscope (Olympus IX71) with a dichroic mirror introduced a 1064 nm NIR laser for optical trapping, reflecting NIR light while transmitting visible light for simultaneous imaging. A 60× objective lens (NA 0.90) focused the NIR laser, with power controlled up to 1.0 W *via* a half-wave plate and polarizing beam splitter. A co-aligned 405 nm UV laser (Thorlabs CPS405) was focused through the same objective. Its power was reduced from 4 mW to <0.04 mW after passing through the optics and fine-tuned using a neutral density filter. Wide-field illumination (100 × 80 μm^2) was achieved by aligning the UV beam parallel to the objective axis. Imaging used a CCD camera (Watec WAT250D), and microspectroscopy employed an Ocean Optics Flame spectrometer with a 200 μm fiber (~3 μm detection area). Optical filters blocked interference from the NIR and UV lasers.

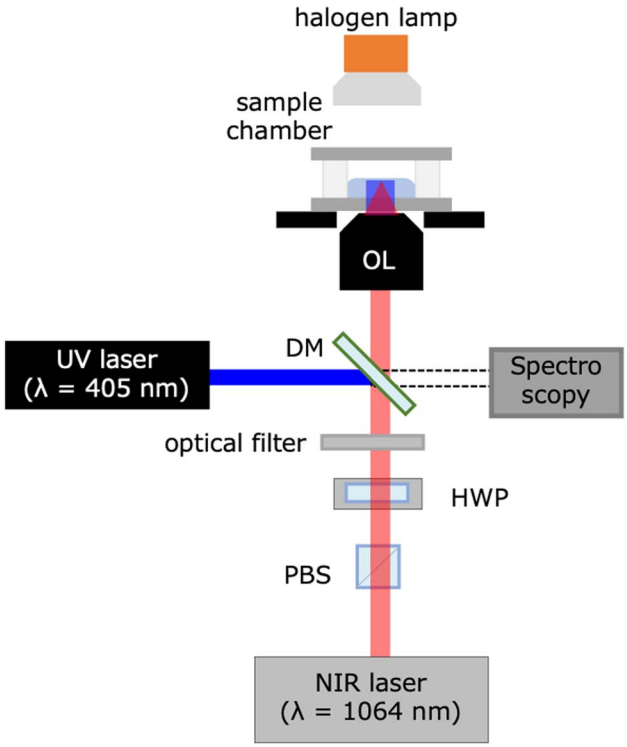

Fig. 2 Optical setup for laser-trapping halide exchange ($MAPbBr_3$ + MAI → $MAPb(Br_{1-x}I_x)_3$) to determine reaction kinetics. A 1064 nm (0.5 W) Nd : YAG laser serves as the trapping source, and a 405 nm (4 mW) laser was used for emission imaging. PBS = polarizing beam splitter; HW = half-wave plate; DM = dichroic mirror.

2.3. Experimental: set of photophysical measurement during halide exchange dynamics

Microspectroscopic analysis involved detecting transmitted light or photoluminescence (PL) using a spectrometer. Absorbance spectra were recorded from 240 nm to capture high-energy transitions of MAI and solvents, as well as any features affecting halide exchange kinetics. Transmission spectra of perovskite crystals were obtained by dividing the white-light spectrum after reaction (I_{cryst}) by a reference spectrum (I_{ref}), canceling dichroic mirror effects.

PL was generated *via* one-photon UV and two-photon NIR excitation. Two-photon excitation was achieved using a tightly focused continuous-wave NIR laser, with the high photon density at the focal spot mimicking pulsed-laser conditions. PL signals were corrected for the dichroic mirror's transmittance. For imaging, samples were observed in transmission (halogen lamp) and PL (wide-field UV laser) modes, captured by a CCD camera at video rates. Low-magnification objectives (×4, NA 0.1; ×10, NA 0.3) were used for larger fields of view.

2.4. Experimental data analysis

To determine the bandgap of the synthesized materials, we collected emission spectra and subsequently converted them

into bandgap in eV. The ratio of I in $MAPbBr_{1-x}I_x$ is calculated using eqn (3). We acknowledge that PL-derived bandgaps can be influenced by Stokes shift and trap-state emission. Although absorbance-based Tauc plots provide more direct bandgap values, limitations in signal intensity and scattering from single microcrystals made such analysis challenging in this setup. However, we performed transmission measurements (I_{ref} *vs.* I_{cryst}) to support the PL results and are developing a combined trapping–UV-vis system for future studies.

We recognize that estimating temperature rise from bubble formation provides only an indirect upper bound of the local temperature. To improve accuracy, future experiments will employ Raman thermometry of the solvent or crystal lattice to obtain direct, real-time temperature profiles during laser irradiation.

The incorporation of iodine inside the $MAPbBr_3$ was directly proportional to the decrease of concentration of reactant MAI. By employing Microsoft Excel, we were able to analyze the data, identify trends, and calculate the equivalent concentration changes associated with the measured iodine ratio progress.

3. Results and discussion

To study halide exchange kinetics in hybrid perovskites, we used a standard halogen exchange reaction. $MAPbBr_3$ crystals (~5 × 5 μm) were synthesized *via* solvent evaporation of a DMF precursor solution containing MABr and $PbBr_2$ in a custom 30 mL glass–silicone reaction chamber. Excess solvent was removed with tissue, and the chamber was placed on an inverted microscope (IX70) stage. Spectroscopic measurements of both pristine and halide-exchanged crystals were performed using a mercury lamp, while the solid $MAPbBr_3$ crystal was illuminated with a 1064 nm continuous-wave laser.

A 0.5 W NIR laser, focused through a 60×, high-NA objective, enabled precise control and *in situ* monitoring of the halide exchange process (Fig. 2). Prior to laser irradiation, the as-grown $MAPbBr_3$ crystal was characterized by transmission and emission spectroscopy, showing a broad absorption edge at 540 nm and a sharp green emission peak at 540 nm (FWHM 30 nm). A reaction solution of 110 μM MAI in IPA/hexadecene (1 : 30, v/v) was then introduced into the chamber. The continuous laser irradiation was then directed onto the target crystal, inducing the halide exchange process. Microscopic imaging additionally spectroscopic analysis with the XRD analysis results of freshly synthesis $MAPbBr_3$ perovskite crystals were illustrated in the Fig. 3. These data revealed the successful synthesis of initial perovskite crystal. Before halide exchange $MAPbBr_3$ shows characteristic green color emission at 540 nm and after addition of iodide ion onto the $MAPbBr_3$ crystal it shows red emission. The transmission image (Fig. 3a) shows the crystal structure using white light on a bright background, while the emission images (Fig. 3b and c) display photoluminescence under UV excitation, where the black background enhances contrast and highlights the emission color change due to Br-to-I substitution.

To optimize the halide exchange reaction, a concentration-dependent study (controlled experiment) was conducted. Control experiments with and without laser trapping revealed a critical concentration threshold. At concentrations below 110 μM of the halide source (MAI), no significant red color change (indicative of iodide incorporation) was observed in the green-emitting $MAPbBr_3$ perovskite within 30 minutes Fig. 4.

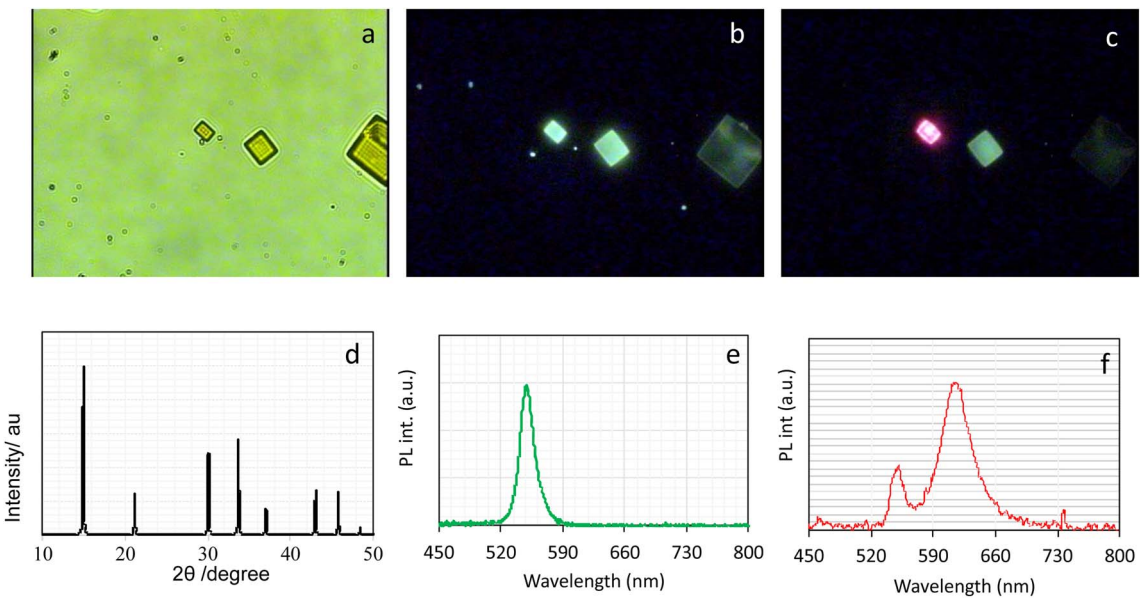

Fig. 3 Characterization of $MAPbBr_3$ crystals and halide-exchange products: (a) transmission microscopy of a $MAPbBr_3$ crystal grown *via* solvent evaporation. (b) Emission image before halide exchange. (c) Emission image of $MAPb(Br_{1-x}I_x)_3$ after laser-induced halide exchange with 110 μM MAI in IPA/hexadecene (1 : 100, v/v). (d) XRD pattern of $MAPbBr_3$. (e) Emission spectrum before exchange. (f) Emission spectrum after exchange. Note: Halide exchange was induced using a 0.5 W continuous-wave laser for 30 min with a 60×, 0.9 NA objective. All images: 35 × 45 μm^2; target crystal: 5 × 5 μm^2.

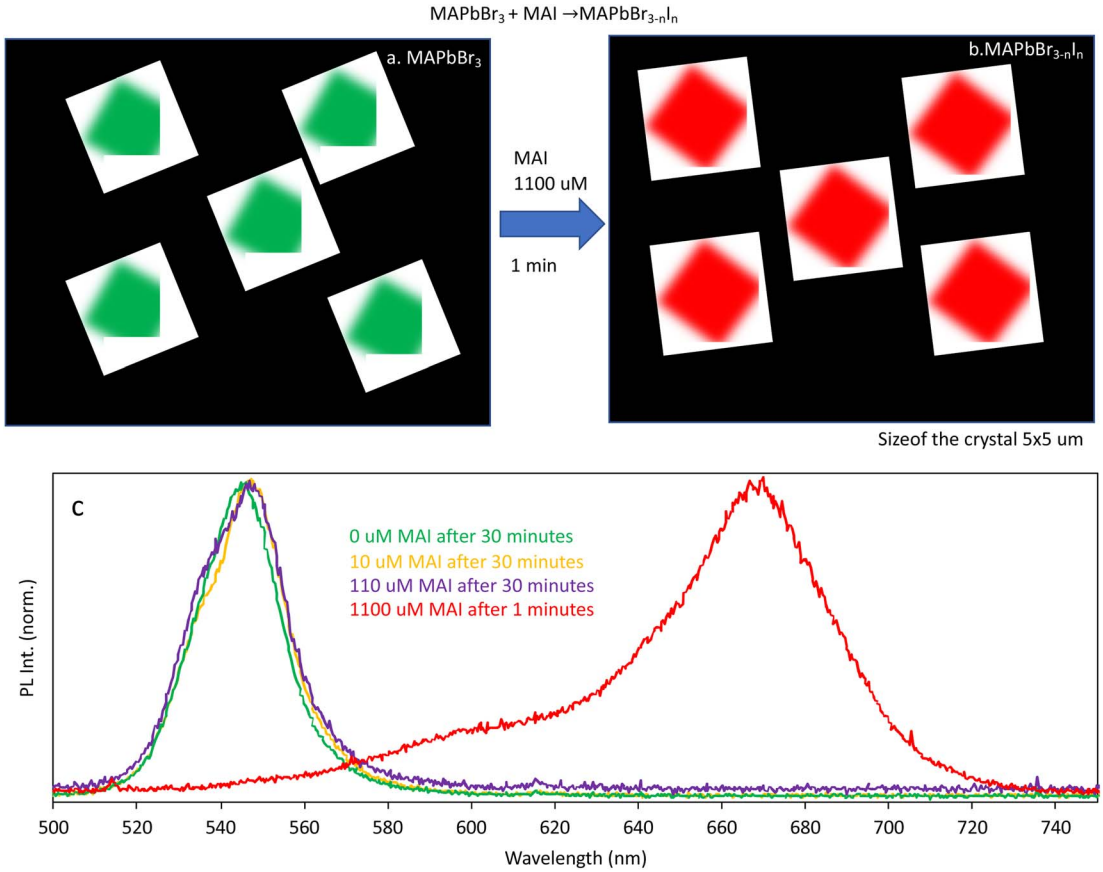

Fig. 4 Optimization of halide exchange parameters for laser-trapping-controlled reaction: (a and b) complete conversion of green-emitting $MAPbBr_3$ to red-emitting $MAPb(Br_{1-x}I_x)_3$ within 1 min upon addition of 1100 μM MAI in IPA/hexadecene. (c) Emission spectra with varying MAI concentrations: 0 μM (green), 10 μM (yellow), 110 μM (violet) after 30 min—no red-shift; 1100 μM (red) after 1 min—red-shift from 540 to 680 nm observed.

Conversely, at higher concentrations 1100 μM, spontaneous halide exchange occurred throughout the entire sample, hindering precise control over the reaction within a specific region. Therefore, an MAI concentration of 110 μM was selected for subsequent laser trapping experiments, providing a suitable balance between efficient halide exchange and spatial control within the laser focus of MAI for conducting laser trapping induced halide exchange reaction.

Isopropyl alcohol, while suitable for dissolving MAI, was not ideal for the stability of $MAPbBr_3$ crystals. The strong absorption of NIR laser light at 1064 nm by the O–H stretching band of isopropyl alcohol leads to rapid temperature elevation, potentially causing the explosion of the target crystal. To mitigate this issue, it was crucial to employ solvents that exhibit minimal absorption at the laser wavelength. Hexadecane, with its lower absorption coefficient, is a more suitable solvent for the dilution of the MAI solution. During the reaction, $MAPbBr_3$ crystals gradually shift from bright green to a lighter red emission, indicating halide exchange in which bromide ions (Br^-) are replaced by other halides such as chloride (Cl^-) or iodide (I^-).

In Fig. 5a, while some broadening of the PL peak was observed during extended laser exposure, we attribute this effect to halide inhomogeneity in the mixed halide region rather than laser-induced crystal damage. XRD patterns (Fig. 3d) confirmed structural integrity, and optimized laser power was maintained at levels that avoided ablation or explosive degradation. Nonetheless, we acknowledge that high-resolution techniques like time-resolved PL or Raman analysis will be required in future work to fully exclude laser-induced defect formation.

Bandgap of the $MAPb(Br_{1-x}I_x)_3$ change with the ratio of Iodine, can be expressed following the equation given below:

$$E_g\{MAPb(Br_{1-x}I_x)_3\} = (1-x) \times E_g(MAPbBr_3) + x \times E_g(MAPbI_3) - b \times x \times (1-x) \quad (5)$$

Here, E_g – Bandgap of Br/I mixed halide perovskites, $E_g(MAPbBr_3) = 2.29$ eV, $E_g(MAPbI_3) = 1.6$ eV. b is bowing constant whose value is 0.57 eV.

The iodine(I) ratio in $MAPb(Br_{1-x}I_x)_3$, corresponding to various emission peaks observed during the halide exchange reaction, was determined using eqn (3).

$$E_g\{MAPb(Br_{1-x}I_x)_3\} = (1-x) \times E_g(MAPbBr_3) + x \times E_g(MAPbI_3) - b \times x \times (1-x)$$

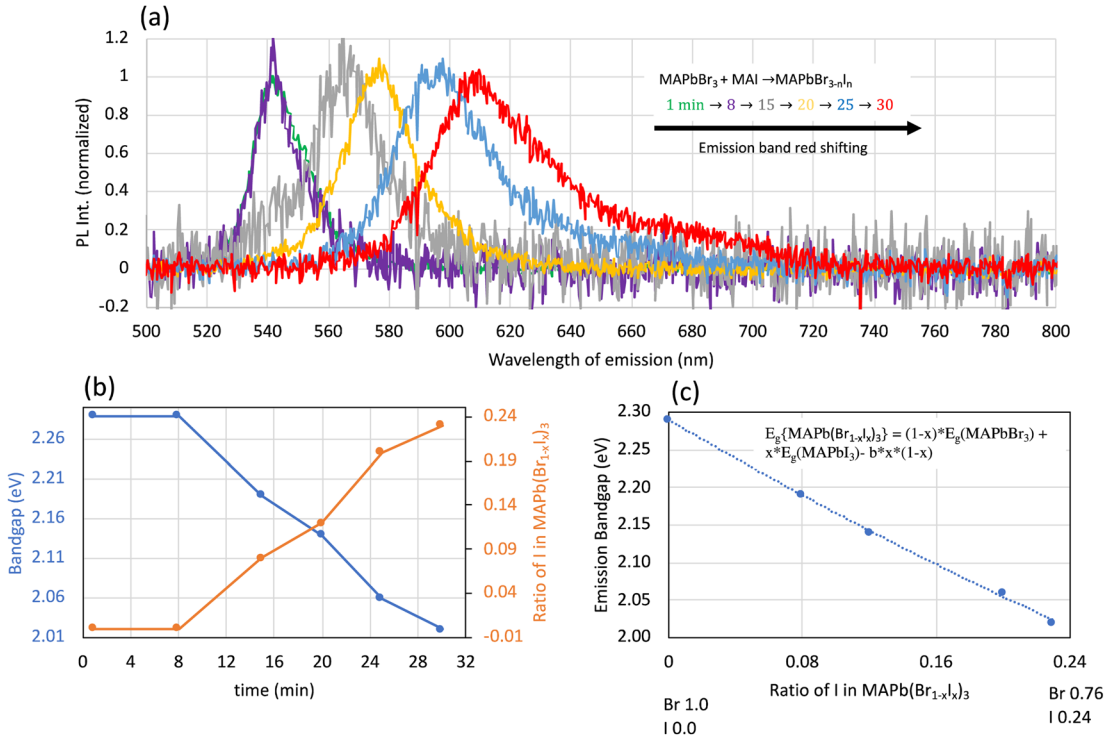

Fig. 5 Progress of the halide exchange reaction (MAI + $MAPbBr_3$ → $MAPb(Br_{1-x}I_x)_3$) for reaction rate and order determination: (a) emission band red-shifts over time. (b) Corresponding bandgap narrows as iodine content increases. No red-shift or bandgap change is observed during the first 8 minutes of the reaction. (c) Change of bandgap with the ratio of iodine in $MAPb(Br_{1-x}I_x)_3$ following the equation $E_g\{MAPb(Br_{1-x}I_x)_3\} = (1-x) \times E_g(MAPbBr_3) + x \times E_g(MAPbI_3) - b \times x \times (1-x)$. Photoluminescence spectra were acquired using 540 nm excitation generated *via* two-photon absorption of the 1064 nm trapping laser.

$$\text{At } 566 \text{ nm} \equiv 2.19 \text{ eV} = (1-x) \times 2.29 + x \times 1.6 - 0.57 \times x \times (1-x);\ x = 0.08$$

$$\text{At } 578 \text{ nm} \equiv 2.14 \text{ eV} = (1-x) \times 2.29 + x \times 1.6 - 0.57 \times x \times (1-x);\ x = 0.12$$

$$\text{At } 600 \text{ nm} \equiv 2.06 \text{ eV} = (1-x) \times 2.29 + x \times 1.6 - 0.57 \times x \times (1-x);\ x = 0.20$$

$$\text{At } 612 \text{ nm} \equiv 2.02 \text{ eV} = (1-x) \times 2.29 + x \times 1.6 - 0.57 \times x \times (1-x);\ x = 0.23$$

This observation is in good agreement with prior studies where progressive halide substitution was shown to induce controlled bandgap narrowing in hybrid perovskite systems.[19] The halide exchange reaction between MAI and $MAPb(Br_{1-x}I_x)_3$, monitored by bandgap changes, reveals a time-dependent incorporation of iodide ions. Importantly, control experiments at the same MAI concentration (110 μM) but without laser irradiation showed no detectable halide exchange over 30 minutes, as evident in Fig. 4. In contrast, laser-irradiated regions exhibited localized, time-dependent red-shifted PL. This suggests that the laser's optical gradient field contributes to a localized MAI concentration increase—likely by trapping molecular clusters, as supported by DLS data in Fig. 7b. The highly selective reaction region, with neighboring crystals remained unchanged, further supports the role of optical trapping over spontaneous diffusion. Initially, at time zero, MAI was considered 100% with a corresponding bandgap of 2.29 eV, indicating no iodide incorporation. Even after 8 minutes of reaction time, no significant change was observed, with the bandgap remaining at 2.29 eV and it was presumed the MAI was still 100%. However, at 15 minutes, the bandgap shifted to 2.19 eV, reflecting a 8% incorporation of iodide ions, leaving 92% of the original MAI. After 30 minutes, the bandgap decreased to 2.02 eV, corresponding to ~23% iodide incorporation and a remaining MAI concentration of 77%. Calculated bandgap changes, iodide incorporation, and MAI consumption were summarized in Table 1. Near-zero values in Table 2

Table 1 Illustration of the extent of the laser trapping-induced halide exchange reaction by presenting the elemental mapping of the ingredients, which confirms the compositional change to $MAPb(Br_{1-x}I_x)_3$ in the hybrid lead halide perovskite formed from solid $MAPbBr_3$ and liquid MAI

Compound	Mass percentage	
Atom	$MAPbBr_3$	$MAPb(Br_{1-x}I_x)_3$
Pb	46.3%	43.23%
Br	53.7%	38.51%
I	0%	18.27%
Total	100%	100%

Table 2 Time dependent parameter change for kinetic analysis, rate and order determination of the laser trapping induced halogen exchange reaction of MAI (l)+ $MAPbBr_3$ (s) → $MAPb(Br_{1-x}I_x)_3$(s)[a]

Time/min	Emission peak/nm	Emission peak/eV	Ratio (x) of [I^-] incorporation	Consumed (%) of [MAI]	Remaining (%) of [MAI] ≡ A_t	ln A_t	$1/A_t$	Absolute concentration of remaining MAI (M)
1	542	2.29	0	0	100	4.605170186	0.0100000	0.0001100
8	542	2.29	0	0	100	4.605170186	0.0100000	0.0001100
15	566	2.19	0.08	8	92	4.521788577	0.01086957	0.0001012
20	578	2.14	0.12	12	88	4.477336814	0.01136364	0.0000968
25	600	2.06	0.2	20	80	4.382026635	0.01250000	0.0000880
30	612	2.02	0.23	23	77	4.343805422	0.01298701	0.0000847

[a] Note: 2.29 eV = initial bandgap of $MAPbBr_3$, A_t ≡ equivalent to concentration of the reactant MAI; absolute initial concentration of MAI is 110 μm. To avoid issues encountered with logarithmic plotting, we present the data using relative values instead of absolute concentrations.

indicate MAI depletion, confirming that iodide incorporation was nearly complete and the reaction slows down due to limited iodine, consistent with zero-order kinetics. The reaction reaches saturation within ~30 minutes, as MAI falls below the threshold needed for further exchange, illustrated by emission red-shifts in Fig. 5.

The initial 0–8 min induction period acts as the rate-determining step. $MAPbX_3$ crystals contain inherent iodide vacancies, which were initially filled by incoming iodide ions to establish a concentration gradient for Br-to-I exchange. The low MAI concentration (110 μM) and sub nanometer size limit its accumulation at the laser focal point, delaying the reaction. Once the threshold is reached, the exchange accelerates and proceeds rapidly.

The emission spectra of the crystals were monitored at regular intervals during the halide exchange reaction. The progressive red-shift in the emission band confirms the ongoing halide exchange process. Pure $MAPbBr_3$ and $MAPbI_3$ crystals exhibit distinct emission bands with emission peak at approximately 540 nm (2.29 eV) and 780 nm (1.6 eV), respectively. This difference in bandgap energy is attributed to the different halide ions, with bromide-based perovskites generally having higher bandgaps than iodide-based perovskites.

We evaluated the laser-trapping-induced halide exchange reaction using EDS elemental mapping to track the change in the bromine and iodine ratio relative to the lead content (Table 1). Initially, the $MAPbBr_3$ crystal showed a Br : Pb atomic molar ratio of approximately 3 : 1 (Pb 46.3% and Br 53.7% mass percentages). After a 30-minute incorporation period with iodide ions, elemental mapping revealed a distinct compositional shift. The bromine content dropped to 38.51%, and the iodine content rose to 18.27%, while the lead value stabilized at 43.23%. This clear change in the Br/I ratio strongly supports the halide exchange process and the resulting formation of the mixed-halide perovskite, with composition of $MAPbBr_{2.31}I_{0.69}$. The EDS spectrum confirmed the presence of the constituent elements, displaying characteristic peaks for lead at 2.345 keV (Mα), 10.551 keV (Lα), and $L\beta_1$ = 12.6137 keV; Bromine at 11.924 keV (Kα), and iodine at 3.937 keV (Lα) (Fig. 6).

Due to the large concentration difference between solid $MAPbBr_3$ and micromolar MAI solution, the reaction can be approximated as a unimolecular process, focusing on the consumption of MAI. The excess $MAPbBr_3$ maintains a constant concentration, while MAI undergoes significant changes. The reaction rate is thus expressed as Rate = $-(d[A])/dt = k[A_t]^n$, where A_t is the MAI concentration at time t, and n is the reaction order. The change in $MAPb(Br_{1-x}I_x)_3$ bandgap serves as an indirect measure of MAI consumption, linking optical properties to reaction kinetics, as further explored through different reaction orders in Table 1.

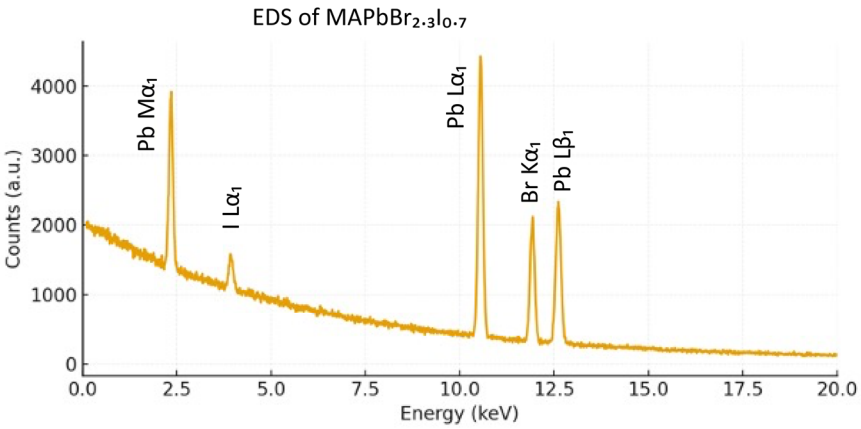

Fig. 6 EDS of $MAPb(Br_{1-x}I_x)_3$ observed in the halide exchange reaction induced by laser trapping.

The initial 0–8 min induction period likely reflects the time needed for iodide ions to accumulate at the laser focal point and to fill intrinsic vacancies in the $MAPbBr_3$ lattice. At low precursor concentration and sub nanometer MAI aggregates, optical trapping initially enriches the local environment slowly. Once a critical threshold of iodide concentration and vacancy occupancy is reached, rapid Br-to-I exchange is initiated, leading to the observed acceleration after 8 min.

After 30 minutes of continuous laser irradiation, the $MAPbBr_3$ crystal exhibited a pronounced red-shift in its transmittance edge from 540 nm to 610 nm, corresponding to a composition of $MAPbBr_{2\cdot3}I_{0\cdot7}$ and indicating selective halide exchange. Other crystals in the solution showed negligible changes, demonstrating the specificity of the laser-induced process. Reaction progress was tracked *via* emission red-shifts, which were converted to bandgap values to determine iodine incorporation at different stages. Based on the solid-state nature of $MAPbBr_3$ and its high concentration relative to MAI, the reaction kinetics follow zero-order behavior.

The concentration of $MAPbBr_3$ was assumed to remain constant during the halide exchange reaction, as the excess amount ensured that it did not significantly deplete. This assumption simplifies the reaction kinetics to a zero order reaction, where the rate does not depends primarily on the concentration of MAI. To determine the exact order of the reaction, the data was fitted to zero-order, first-order, and second-order rate equations. To test whether the observed zero-order behavior was truly laser-induced, we conducted control experiments at 110 μM MAI without laser exposure. No observable bandgap change occurred within 30 minutes, indicating that optical trapping was essential for surpassing the local concentration threshold necessary to initiate the reaction. However, at 1100 μM MAI, spontaneous halide exchange was observed without laser, although this process lacked spatial selectivity and control. We plan to expand these control studies in future work to fully map kinetic behavior under non-trapped conditions.

The highest regression coefficient (R^2) was observed for the zero-order rate equation, indicating the closest fit to the experimental data. Compared to earlier kinetic studies involving bulk perovskite systems,[20,21] our laser-induced approach yields zero-order kinetics. This suggests that the reaction rate was independent of MAI concentration once the local accumulation threshold was reached, a behavior made possible by the optical trapping-induced concentration enhancement mechanism. While a perfect match to any specific order was not found, the data strongly suggests a zero-order reaction with respect to MAI. This was supported by the observed reaction behavior: at low MAI concentrations, the reaction proceeds slowly, and the color shift is minimal.[22–24] At higher concentrations, the reaction proceeds rapidly, producing a pronounced color change. The laser-trapping–induced halide exchange kinetics are illustrated in Fig. 7.

By monitoring the emission band changes over time, the reaction rate and half-life were determined. The zero-order

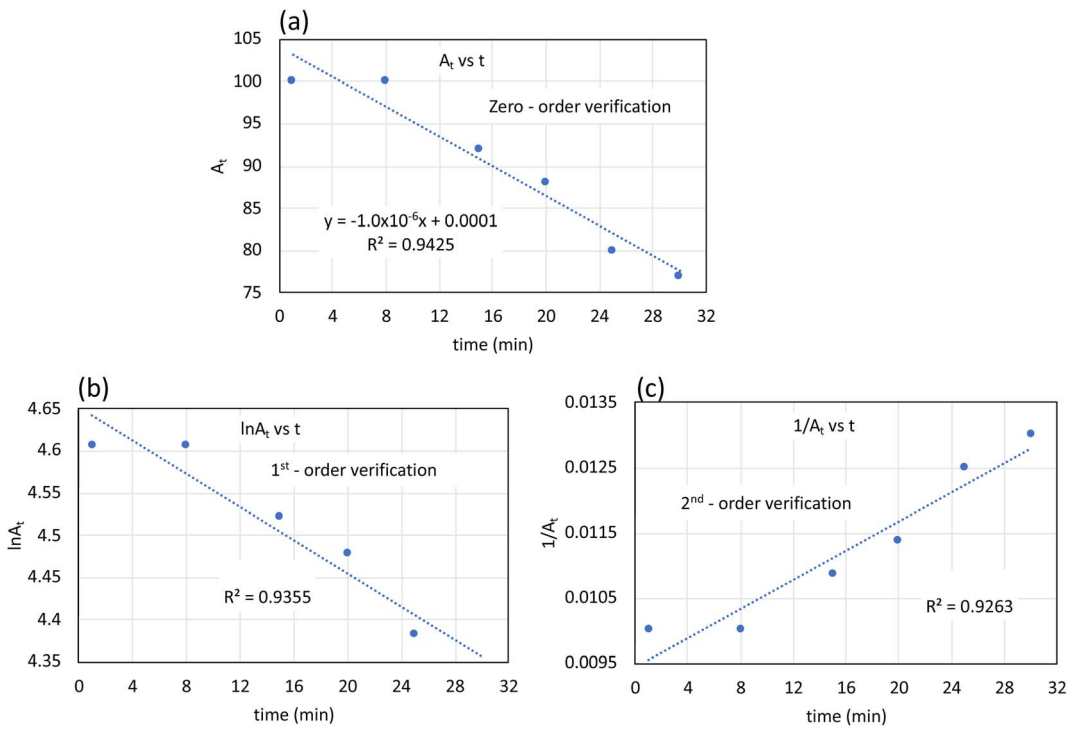

Fig. 7 Verification of the halide exchange reaction order (MAI (l) + $MAPbBr_3$ (s) → $MAPb(Br_{1-x}I_x)_3$ (s)) under 1064 nm CW laser trapping (0.5 W): (a) Plot of concentration (A_t) *vs.* time (t); a straight line indicates zero-order kinetics. (b) Ln A_t *vs.* t; a straight line with negative slope indicates first-order. (c) $1/A_t$ *vs.* t; a straight line with positive slope indicates second-order. Insets show regression values; (a) inset gives the zero-order rate constant, 1.0×10^{-6} M min^{-1}, based on the initial MAI concentration of 110×10^{-6} M.

reaction exhibited a half-life of 55 minutes, indicating a relatively slow reaction rate.

Half-life of the zero order reaction is $t_{1/2} = \frac{[A]_o}{2k}$.

Initial concentration of MAI is 110 μm = 110×10^{-6} M.

The unit of constant is

$$k = \frac{\text{concentration}}{\text{time}} = \frac{\text{mol L}^{-1}}{\text{minute}} = (\text{mol L}^{-1})\text{min}^{-1} = \text{M min}^{-1}$$

Here, rate constant $k = 1.0 \times 10^{-6}$ (M min^{-1})

$$t_{1/2} = \frac{[A]_o}{2k} = \frac{110 \times 10^{-6}\text{M}}{2 \times 1.0 \times 10^{-6}(\text{M per minute})} = 55 \text{ minutes}$$

The halide exchange under focused NIR laser irradiation was driven by a local MAI concentration increase *via* laser trapping. While the optical force cannot trap individual MAI molecules, clusters formed through Brownian motion can be trapped and concentrated at the focal point.[25,26] Then solid–liquid interface at the perovskite crystal surface further allow diffusion, enhancing the local concentration of MAI. While this mechanism provides a plausible explanation, further investigation was needed to fully understand the underlying processes involved in the local concentration elevation and halide exchange reaction. Although the change in $MAPb(Br_{1-x}I_x)_3$ bandgap was used here as an indirect proxy for MAI consumption, this approach assumed a direct correlation between iodide incorporation and emission red-shift. While our dynamic light scattering data (Fig. 7b) supported a local concentration increase *via* optical trapping, future work will employ fluorescently tagged MAI and advanced spectroscopy to directly visualize and quantify the concentration gradients created by the trap.

Fig. 8 provides insights into the characteristics of methylammonium iodide (MAI) in the isopropanol/hexadecane solvent mixture. Dynamic light scattering (DLS) analysis, as shown in Fig. 7b, revealed that the size of MAI in this solution was in the sub nanometer range, indicating the presence of individual ions or small aggregates. Furthermore, Fig. 7a suggests the presence of an absorption band at 1064 nm and a potential two-photon excitation band at 532 nm within the MAI solution. These findings provide crucial information about the physical and optical properties of MAI in the reaction medium, which are essential for understanding the subsequent laser-induced halide exchange processes. Here it is mentionable, during the transmittance measurement, around 5% light loss by reflection form the air/glass interface.

While the 1064 nm trapping laser exhibits possible absorption by the MAI precursor solution along with solid $MAPbBr_3$ crystal due to the presence of an absorption band at that wavelength, we investigated the influence of temperature on the halide exchange kinetics of $MAPbBr_3$ to $MAPb(Br_{1-x}I_x)_3$ Fig. 7.

To assess temperature, rise during halide exchange, the $MAPbBr_3$ crystal was irradiated with a focused 1064 nm NIR laser, inducing two-photon absorption as confirmed by emission. The non-radiative relaxation of absorbed energy generates a localized temperature increase at the laser focal point.[27,28] To estimate this temperature rise, the study utilized the concept of spinodal temperature (T_s) concept, the temperature limit beyond which a metastable liquid (in this case, isopropyl alcohol with a T_s of 239 °C) becomes unstable and undergoes rapid phase transition. By observing bubble formation in isopropyl alcohol surrounding the laser-irradiated $MAPbBr_3$ crystal, the study inferred that the localized temperature at the focal spot exceeded the spinodal temperature of the solvent, providing an indirect measure of the temperature rise induced by the two-photon absorption process in the $MAPbBr_3$ crystal.

The effect of temperature on the halide exchange in $MAPbBr_3$ crystals was examined using a 1100 μM MAI solution in a hexadecane:isopropanol mixture. The reaction conducted at elevated temperatures is shown in Fig. 9.

In temperature dependent halide exchange spontaneous reaction, $MAPbBr_3$ crystals were exposed to a 1100 μM MAI solution at varying temperatures (18, 70, 100, 150 °C) for 5 minutes. The melting point of solvent 1-hexadecene is 5 °C. At 18 °C, a green-to-red emission (Fig. 8.a.i) shift (halide exchange) was observed *via* photoluminescence (PL) imaging. However, at elevated temperatures, the crystals retained their green emission (Fig. 9a(ii–iv)), indicating suppression of halide exchange. Fig. 9b shows the corresponding emission band shift at varying temperatures (18, 70, 100, 150 °C). Heating suppresses a reaction involving MAI, as evidenced by absorption spectra showing

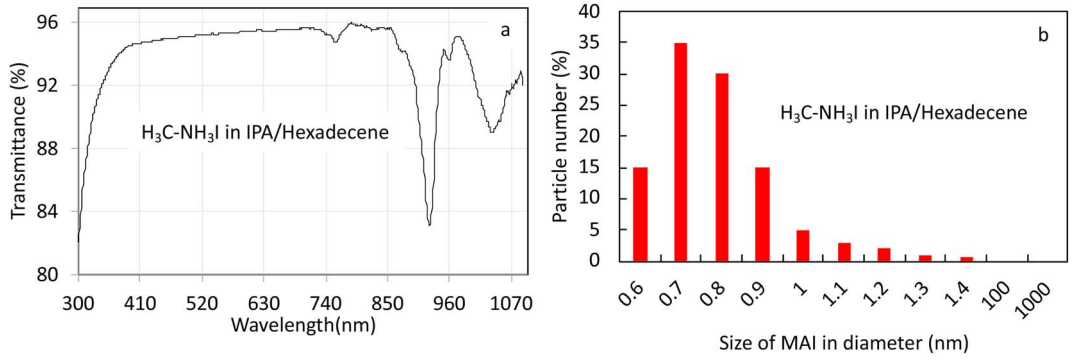

Fig. 8 (a) UV-vis-NIR absorption spectrum of the MAI solution in the isopropanol/hexadecane mixed solvent. (b) Dynamic Light Scattering (DLS) measurements of the methyl ammonium iodide (MAI) precursor particle size distribution in the isopropanol/hexadecane solution used for laser trapping-controlled halide exchange reactions.

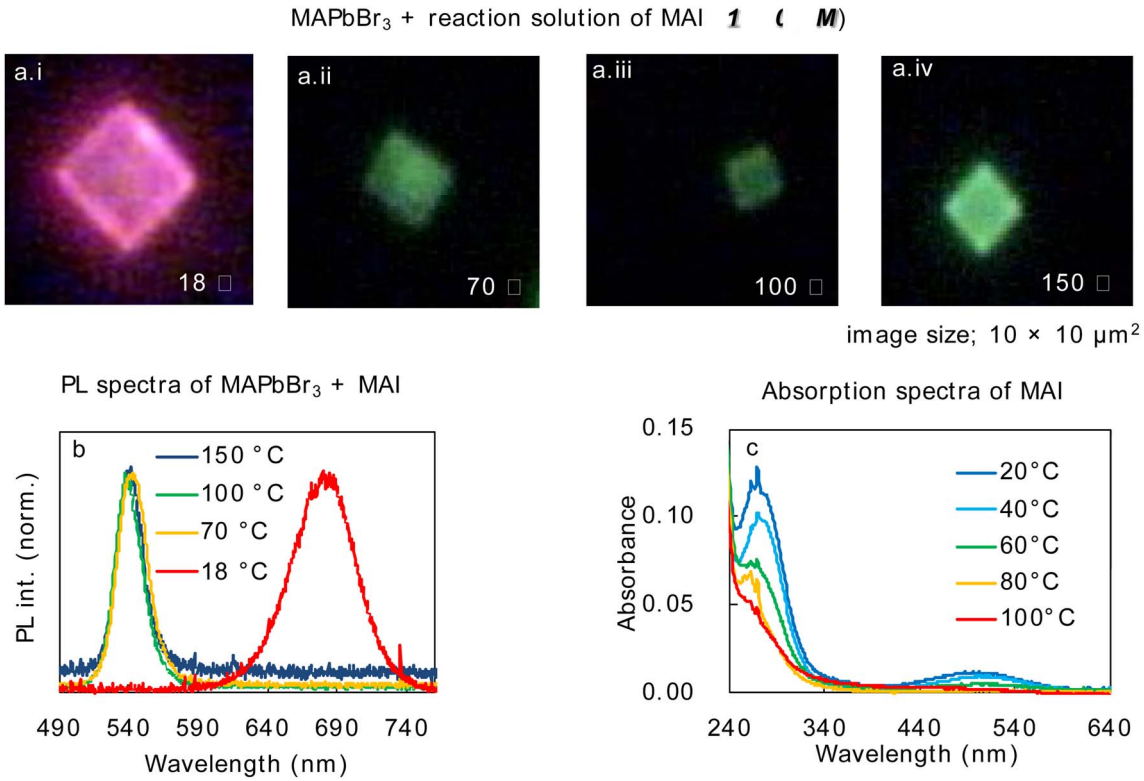

Fig. 9 Temperature-dependent halide exchange in $MAPbBr_3$ crystals: (a) PL images show green-to-red emission shift at 18 °C (i), while green emission is retained at 70 °C (ii), 100 °C (iii), and 150 °C (iv), indicating suppressed exchange. (b) Emission spectra of $MAPbBr_3$ + MAI at different temperatures. (c) Absorption spectra show disappearance of the MAI peak (450–550 nm) at higher temperatures, reflecting accelerated MAI evaporation and reduced iodide availability, which inhibits halide exchange.

the disappearance of MAI characteristic peak (450–550 nm) at higher temperatures (Fig. 9c). This suggests accelerated MAI evaporation, reducing iodide ion concentration. This observation is more accurately attributed to evaporation of isopropanol (IPA), not MAI itself, given MAI's negligible volatility. IPA's low boiling point (~82.5 °C) and MAI's limited solubility in hexadecane likely result in phase separation or precipitation, reducing effective iodide concentration. We have revised the interpretation accordingly. Consequently, the halide exchange reaction with $MAPbBr_3$ crystals is inhibited at elevated temperatures due to insufficient iodide ions.

Halide exchange experiments were performed in hexadecene, a low-thermal-conductivity solvent (0.085 W m^{-1} K^{-1}) compared to isopropanol (0.14 W m^{-1} K^{-1}).[29] This caused a significant local temperature rise (~61 K) under laser irradiation, with the crystal surface reaching ~80 °C. As elevated temperatures suppress halide exchange, the two-photon–induced heating likely inhibited the reaction at the focal spot. To provide direct confirmation of the temperature elevation previously inferred from indirect chemical measurements of MAI thermal dissociation, we utilized a remote sensing NIR active thermometer (Micro IR-200 Infrared Thermometer). Under identical experimental conditions, a 1064 nm NIR trapping laser operating at 500 mW was focused into a reaction solution containing $MAPbBr_3$. Five repeated measurements of the temperature at the laser's focal spot yielded readings of 78, 79, 79, 79, and 81 °C. This consistent and significant local temperature increase directly authenticates the conditions—specifically the high localized heating—evolved during the laser trapping induced halide exchange reaction for kinetics analysis.

The vacancy-assisted halide exchange in hybrid lead halide perovskites occurs *via* a multi-step process.[30,31] Halide ions from the precursor solution rapidly diffuse into the perovskite lattice, but the accumulation of iodide at the laser focal point was slower. Once a threshold iodide concentration was reached, the exchange begins, though an extended induction period occurs due to the low concentration and small size of MAI, limiting its trapping. Vacancies in the lattice facilitate ion migration, allowing incoming halides to displace original ions, altering the crystal's composition and optical properties. The exchange rate depends on precursor concentration, temperature, halide type, and lattice vacancy density, with higher vacancy concentrations accelerating ion diffusion and reaction kinetics.[32,33]

Here, we employed laser trapping to induce halide exchange reactions, offering a unique platform for investigating chemical kinetics and developing novel optical manipulation techniques. This non-contact approach allows for precise control over the reaction zone, enabling the acceleration of chemical reactions within a specific region while leaving the surrounding area undisturbed. This capability is particularly valuable for manipulating multi-color emitting perovskites, where the precise control of halide ion concentrations is crucial for tuning

their emission properties. By implementing laser trapping, we can selectively modify the composition and optical properties of perovskite nanocrystals within a complex mixture. The bandgap evolution trend we observed experimentally aligns with computational predictions of halide exchange effects on electronic structure in perovskites.[34,35]

4. Conclusion

We performed a laser-trapping–induced halide exchange to study the kinetics in $MAPbBr_3$ single crystals ($\sim 5 \times 5$ μm) prepared *via* solvent evaporation from DMF. Crystals were irradiated with a 0.5 W, 1064 nm continuous-wave laser, while a 10 mL solution of 110 μM MAI in IPA/hexadecene served as the iodide source. MAI gradually accumulated at the laser focal point, enabling iodide ions to replace bromide ions at the solid–solution interface, forming $MAPb(Br_{1-x}I_x)_3$. Monitoring luminescence spectra allowed tracking of bromide and iodide emission peaks. After 30 min of irradiation, the emission redshifted from 540 nm to 612 nm, corresponding to a bandgap change from 2.29 eV to 2.02 eV, indicating formation of $MAPbBr_{2.3}I_{0.7}$. Bandgap changes were correlated with reactant concentration to construct concentration–time plots. Comparison of zero-, first-, and second-order fits indicated closest agreement with zero-order kinetics, yielding a rate constant of 1.0×10^{-6} M min^{-1} and a half-life of 55 min. These results demonstrate that laser trapping serves as a precise and versatile tool for studying chemical kinetics while simultaneously enabling spatial control over halide composition. Such capability opens new opportunities for site-specific bandgap engineering in perovskite-based photonic and photovoltaic devices. Importantly, our findings not only confirm the occurrence of laser-driven halide exchange but also establish, for the first time, its zero-order kinetic nature, thereby providing a mechanistic framework that advances beyond prior phenomenological reports. This novelty underscores the broader potential of optical tweezers as a quantitative probe of ionic transport processes in hybrid perovskites, offering a powerful approach for both fundamental studies and practical applications in next-generation optoelectronic materials.

Conflicts of interest

The authors declare that they have no conflict of interests related to this research study.

Data availability

The data that support the findings of this study, including spectroscopic measurements, kinetic analyses, and raw experimental data, are available from the corresponding author upon reasonable request.

Acknowledgements

We sincerely thank Professors Ken-ichi Yuyama (Osaka City University) and Vasudevanpillai Biju (Hokkaido University) for their guidance, discussion, and support in planning the reaction. We also acknowledge Professor H. Misawa, K. Ueno, and T. Oshikiri (Hokkaido University) for their crucial experimental assistance with the 1064 nm laser. This work was supported by the MEXT JSPS Grant-in-Aid for Scientific Research for Young Scientists (Grant No. 17K14427, to KY) and the Grant-in-Aid for Scientific Research on Innovative Areas (Grant No. 17H01099, to VB). We are grateful to the MEXT Dynamic Alliance for Open Innovation Bridging Human, Environment, and Materials for enabling the successful completion of this project.

References

1 C. J. Taylor, A. Pomberger, K. C. Felton, R. Grainger, M. Barecka, T. W. Chamberlain, R. A. Bourne, C. N. Johnson and A. A. Lapkin, A brief introduction to chemical reaction optimization, *Chem. Rev.*, 2023, **123**(6), 3089–3126.

2 R. Zenteno-Catemaxca, J. G. Moguel-Castañeda, V. M. Rivera, H. Puebla and E. Hernandez-Martinez, Monitoring a chemical reaction using pH measurements: An approach based on multiscale fractal analysis, *Chaos, Solitons Fractals*, 2021, **152**, 111336.

3 P. Coatsworth, L. Gonzalez-Macia, A. S. Collins, T. Bozkurt and F. Güder, Continuous monitoring of chemical signals in plants under stress, *Nat. Rev. Chem.*, 2023, **7**(1), 7–25.

4 C. Gao, Q. Gao, C. Zhao, Y. Huo, Z. Zhang, J. Yang, C. Jia and X. Guo, Technologies for investigating single-molecule chemical reactions, *Natl. Sci. Rev.*, 2024, **11**(8), nwae236.

5 M. J. Islam and M. H. Islam, Tuning emission and bandgap dynamics of $MAPbBr_3$ single crystals through halide exchange with methyl iodide, *Chem. Phys. Impact*, 2025, **10**, 100807.

6 J. Liu and Z. Li, Controlled mechanical motions of microparticles in optical tweezers, *Micromachines*, 2018, **9**(5), 232.

7 Y. Ren, Q. Chen, M. He, X. Zhang, H. Qi and Y. Yan, Plasmonic optical tweezers for particle manipulation: principles, methods, and applications, *ACS Nano*, 2021, **15**(4), 6105–6128.

8 Z. Chen, Z. Cai, W. Liu and Z. Yan, Optical trapping and manipulation for single-particle spectroscopy and microscopy, *J. Chem. Phys.*, 2022, **157**(5), 807–819.

9 C. Otero-Martínez, M. Imran, N. J. Schrenker, J. Ye, K. Ji, A. Rao, S. D. Stranks, R. L. Hoye, S. Bals, L. Manna and J. Pérez-Juste, Fast A-site cation cross-exchange at room temperature: single-to double-and triple-cation halide perovskite nanocrystals, *Angew. Chem., Int. Ed.*, 2022, **61**(34), e202205617.

10 Y. Zhang, D. Lu, M. Gao, M. Lai, J. Lin, T. Lei, Z. Lin, L. N. Quan and P. Yang, Quantitative imaging of anion exchange kinetics in halide perovskites, *Proc. Natl. Acad. Sci. U. S. A.*, 2019, **116**(26), 12648–12653.

11 H. Yuan, E. Debroye, E. Bladt, G. Lu, M. Keshavarz, K. P. Janssen, M. B. Roeffaers, S. Bals, E. H. Sargent and J. Hofkens, Imaging heterogeneously distributed photo-

active traps in perovskite single crystals, *Adv. Mater.*, 2018, **30**(13), 1705494.

12 M. J. Islam, M. Shahjahan, K. I. Yuyama and V. Biju, Remote tuning of bandgap and emission of lead perovskites by spatially controlled halide exchange reactions, *ACS Mater. Lett.*, 2020, **2**(4), 403–408.

13 M. J. Islam, K. Pal, M. Harun-Ur-Rashid, A. Kumar, M. F. Hossain, N. Asthana, S. Rajendran, S. Vallinayagam and A. Malik, Optical maneuvering of photofunctioning hybrid perovskite for future photonics potential application, *J. Mol. Liq.*, 2024, **408**, 125343.

14 K. Chen, D. Zhang, Q. Du, W. Hong, Y. Liang, X. Duan, S. Feng, L. Lan, L. Wang, J. Chen and D. Ma, Synergistic halide-and ligand-exchanges of all-inorganic perovskite nanocrystals for near-unity and spectrally stable red emission, *Nanomaterials*, 2023, **13**(16), 2337.

15 M. J. Islam, S. Islam and M. H. Islam, Fluorinated ligand enhanced luminescent europium (III) noble complexes for potential application in biomedical field, *Next Mater.*, 2025, **8**, 100936.

16 M. Behloul, E. Salmani, H. Ez-Zahraouy and A. Benyoussef, Theoretical investigation of electronic, magnetic and optical properties of ZnSe doped TM and co-doped with MnTM (TM: Fe, Cr, Co): AB-initio study, *J. Magn. Magn. Mater.*, 2016, **419**, 233–239.

17 M. J. Islam, N. Sayara, T. Talukder and M. Harun-Ur-Rashid, Trapping light, revealing properties: Laser trapping as a powerful tool for photoluminescence spectroscopy, *Chem. Phys. Impact*, 2024, **9**, 100764.

18 M. Ziati, N. Bekkioui and H. Ez-Zahraouy, Correlation between carrier mobility and effective mass in Sr2RuO4–xFx (x= 2) under uniaxial strain using the Yukawa screened PBE0 hybrid functional, *J. Phys. Chem. Solids*, 2022, **161**, 110409.

19 M. Ziati, N. Bekkioui and H. Ez-Zahraouy, Correlation between carrier mobility and effective mass in Sr2RuO4–xFx (x= 2) under uniaxial strain using the Yukawa screened PBE0 hybrid functional, *J. Phys. Chem. Solids*, 2022, **161**, 110409.

20 M. L. Ould Ne, A. Abbassi, A. G. El Hachimi, A. Benyoussef, H. Ez-Zahraouy and A. El Kenz, Electronic optical, properties and widening band gap of graphene with Ge doping, *Opt. Quantum Electron.*, 2017, **49**(6), 218.

21 M. Ziati, N. Bekkioui and H. Ez-Zahraouy, Ruddlesden-Popper compound Sr2TiO4 doped with chalcogens for optoelectronic applications: Insights from first-principle calculations, *Chem. Phys.*, 2021, **548**, 111221.

22 F. Furlan, D. Nodari, E. Palladino, E. Angela, L. Mohan, J. Briscoe, M. J. Fuchter, T. J. Macdonald, G. Grancini, M. A. McLachlan and N. Gasparini, Tuning halide composition allows low dark current perovskite photodetectors with high specific detectivity, *Adv. Opt. Mater.*, 2022, **10**(24), 2201816.

23 T. A. Berhe, W. N. Su and B. J. Hwang, Halide perovskites' multifunctional properties: coordination engineering, coordination chemistry, electronic interactions and energy applications beyond photovoltaics, *Inorganics*, 2024, **12**(7), 182.

24 M. J. Islam and M. H. Islam, Chemical Wrapping for Selective Crystal Formation Using Trapping Light Induction, *Curr. Appl. Phys.*, 2025, 1–9.

25 N. A. Kattan, Q. Mahmood, G. Nazir, A. Rehman, N. Sfina, M. mana Al-anazy, S. A. Sofi, M. Morsi and M. A. Amin, Modifying electronic bandgap by halide ions substitution to investigate double perovskites Rb2AgInX6 (X= Cl, Br, I) for solar cells applications and thermoelectric characteristics, *Mater. Today Commun.*, 2023, **34**, 105166.

26 D. Amgar, T. Binyamin, V. Uvarov and L. Etgar, Near ultra-violet to mid-visible band gap tuning of mixed cation Rb x Cs 1− x PbX 3 (X= Cl or Br) perovskite nanoparticles, *Nanoscale*, 2018, **10**(13), 6060–6068.

27 M. J. Islam, M. H. Islam and M. Shahid, Accelerated Growth in Laser-Trapped MAPbBr3 Perovskite Crystals, *ChemistrySelect*, 2025, **10**(17), e202501093.

28 A. Chaouiki, M. Chafiq and Y. G. Ko, The art of controlled nanoscale lattices: A review on the self-assembly of colloidal metal–organic framework particles and their multifaceted architectures, *Mater. Sci. Eng. R Rep.*, 2024, **159**, 100785.

29 J. Yang and Y. W. Yang, Metal–organic frameworks for biomedical applications, *Small*, 2020, **16**(10), 1906846.

30 Y. Chen, F. Fang and N. Zhang, Advance in additive manufacturing of 2D materials at the atomic and close-to-atomic scale, *npj 2D Mater. Appl.*, 2024, **8**(1), 17.

31 M. J. Islam and M. H. Islam, Unraveling the role of ligand structure in modulating chiral europium complex luminescence, *Chem. Phys. Impact*, 2025, **10**, 100859.

32 A. P. Anbari, S. R. Delcheh, M. Kashif, A. Ranjbari, M. K. Akbari, P. M. Heynderickx, M. Amini, S. Zhuiykov and F. Verpoort, Recent progress on core-shell zeolitic imidazole frameworks: a review of synthesis and applications, *Comments Inorg. Chem.*, 2025, **45**(4), 361–401.

33 Y. Lei, T. Zhang, Y. C. Lin, T. Granzier-Nakajima, G. Bepete, D. A. Kowalczyk, Z. Lin, D. Zhou, T. F. Schranghamer, A. Dodda and A. Sebastian, Graphene and beyond: recent advances in two-dimensional materials synthesis, properties, and devices, *ACS Nanosci. Au*, 2022, **2**(6), 450–485.

34 M. Benyoussef, H. Zaari, J. Belhadi, Y. El Amraoui, H. Ez-Zahraouy, A. Lahmar and M. El Marssi, Effect of rare earth on physical properties of Na0. 5Bi0. 5TiO3 system: A density functional theory investigation, *J. Rare Earths*, 2022, **40**(3), 473–481.

35 H. Absike, Z. Essalhi, H. Labrim, B. Hartiti, N. Baaalla, M. Tahiri, B. Jaber and H. Ez-Zahraouy, Synthesis of CuO thin films based on Taguchi design for solar absorber, *Opt. Mater.*, 2021, **118**, 111224.